Available online at www.sciencedirect.com
SCIENCE DIRECT®
Journal of Solid State Chemistry 179 (2006) 2067–2078
JOURNAL OF SOLID STATE CHEMISTRY
www.elsevier.com/locate/jssc

Anion substitution effects on structure and magnetism of the chromium chalcogenide Cr_5Te_8—Part II: Cluster-glass and spin-glass behavior in trigonal $Cr_{(1+x)}$ Q_2 with basic cells and trigonal $Cr_{(5+x)}$ Q_8 with superstructures (Q = Te, Se; Te:Se = 6:2)

Zhong-Le Huang[a,*], Wolfgang Bensch[a], Sergiy Mankovsky[b], Svitlana Polesya[b], Hubert Ebert[b], Reinhard K. Kremer[c]

[a]*Institute of Inorganic Chemistry, Christian-Albrechts-University Kiel, Olshausenstr.40, D-24098 Kiel, Germany*
[b]*Department of Chemistry, LMU-Munich, Butenandstr. 5-13, D-81377 Munich, Germany*
[c]*Max-Planck Institut für Festkörperforschung, Heisenbergstr. 1, D-70506 Stuttgart, Germany*

Received 10 February 2006; received in revised form 24 March 2006; accepted 2 April 2006
Available online 17 April 2006

Abstract

The effect of substitution of up to two Te atoms by Se atoms on the crystal structure, the magnetic and electronic properties has been studied in the system $Cr_{(5+x)}Te_{8-y}Se_y$.

Trigonal basic cells with space group $P-3m1$ for $Cr_{(1+x)}Q_2$ and trigonal supercells (doubling of the unit cell in all directions) with space group $P-3m1$ for $Cr_{(5+x)}Q_8$ ($(1+x) = 1.27, 1.32, 1.36$; $(5+x) = 5.08, 5.28, 5.44$; Q = Te, Se; Te:Se = 6:2) have been identified in X-ray powder diffraction patterns and Rietveld refinements as high-temperature and low-temperature phases, respectively. The crystal structures are related to the hexagonal NiAs-type structure with metal vacancies in every second metal layer. The magnetic properties are closely related to the Cr content and the structure type. Cluster-glass and spin-glass behavior at low temperatures are observed for high and low Cr contents, respectively. For the same Cr content, the phases with trigonal basic cells have higher values for the Curie temperature T_c and the freezing temperature T_f, and larger magnetization than those for the phases with trigonal supercells. For the same structure type, the values for T_c/T_f do not show a linear relationship with the change of Cr content but exhibit a V-shape fashion.

Our experimental investigations were accompanied by spin-polarized relativistic Korringa–Kohn–Rostoker (SPR-KKR) electronic structure calculations. Cr deficiencies as well as atomic disorder on the chalcogen sites was accounted for using the coherent potential approximation (CPA) alloy theory. Calculation of the exchange coupling parameters J_{ij} provided the basis for subsequent Monte Carlo simulations of the magnetic properties at finite temperatures.

Keywords: Chromium chalcogenide; Anion substitution; Rietveld refinement; Low field magnetization; Cluster-glass; Spin-glass; Band-structure calculations

1. Introduction

Binary and quasi-binary chromium chalcogenides show a rich variety of magnetic and electrical properties that depend sensitively on the actual stoichiometry and the kind of chalcogenide anion [1–10]. Some of these compounds have been predicted to be excellent half-metallic ferromagnets, a key ingredient in high performance spintronic devices [1].

The chromium tellurides ($Cr_{(1-x)}Te$, Cr_3Te_4, Cr_2Te_3 and the dimorphic Cr_5Te_8) [2] are ferromagnetic metals; chromium selenides ($Cr_{(1-x)}Se$, Cr_3Se_4, Cr_2Se_3, Cr_5Se_8) [3] and sulfides (CrS, Cr_5S_6, Cr_3S_4, Cr_2S_3, Cr_5S_8) [3b,4] are predominantly antiferromagnetic and show either a metallic or semiconducting behavior.

These phases crystallize with ordered defect structures intermediate between the NiAs and the CdI_2 structure

*Corresponding author. Fax: +49 (0)431 880 1520.
E-mail address: zlhuang@ac.uni-kiel.de (Z.-L. Huang).

0022-4596/$ - see front matter © 2006 Elsevier Inc. All rights reserved.
doi:10.1016/j.jssc.2006.04.001

types. Each phase exists within a certain homogeneity range of the Cr content. The different structure types with specific arrangements of metal atom vacancies depend on the actual composition and details of the sample preparation. In general, the presence of structural disorder and competing exchange interactions complicate the elucidation of the magnetic behavior and for many of these phases the magnetic properties have not been investigated so far. In several preceding publications we reported the crystal structures and physical properties of $Cr_{5\pm x}Te_8$ [5,6], $Cr_{5.095}Se_8$ [7], and $Cr_{5+y}S_8$ [8]. Subsequently, we investigated the influence of anion and cation substitution in Cr_5Te_8 phases onto the crystal structure, physical properties and electronic structure. Especially we studied the quasi-binary phases $Cr_{5\pm x}Te_7Se$ and $Cr_{5-x}Ti_xTe_8$ ($0<x<5$) and found remarkable changes of the crystal structures and the magnetic properties [9,10].

The present contribution reports new results of a continuing study of the effect of anion substitution of up to two Te atoms by Se in the non-stoichiometric phases $Cr_{5\pm x}Te_{8-y}Se_y$.

The paper is organized as follows: After a description of the two different structural modifications originating from different synthesis conditions, we present and discuss the results of the magnetic measurements. In the last section the results of accompanying theoretical investigations are discussed. Electronic structure calculations have been performed using the spin-polarized relativistic Korringa–Kohn–Rostoker (SPR-KKR) method in combination with the coherent potential approximation (CPA) within the framework of local spin density approximation (LSDA). Calculations of the exchange coupling constants provided the basis for subsequent Monte Carlo simulations of the magnetic properties at finite temperatures.

2. Experimental

2.1. Synthesis

$Cr_{(1+x)}Q_2$ ($(1+x) = 1.27$, 1.32, 1.36) high temperature phases with trigonal unit cells were prepared by reaction of Cr (99.99%, Heraeus), Te (99.999%, Retorte) and Se (99.95%, Retorte) powders in evacuated silica tubes according to the composition range $Cr{:}Q = 5.00{:}8.00$ – 5.40:8.00. Each starting mixture was heated up to 1223 K at a rate of 20 K/h and held at this temperature for 6 days. The temperature was then decreased to 1073 K at a rate of 100 K/h and held at this temperature for 2 days and finally quenched to room-temperature in a water bath.

$Cr_{(5+x)}Q_8$ ($(5+x) = 5.08$, 5.28, 5.44) low temperature phases with trigonal supercells were prepared by annealing the $Cr_{(1+x)}Q_2$ samples. The annealing procedure was as follows: The $Cr_{(1+x)}Q_2$ samples were loaded in evacuated silica tubes. The temperature was raised to 1223 K at a rate of 100 K/h and held at this temperature for 2 days. Then the temperature was decreased to 723 K at a cooling rate of 20 K/h and held at this temperature for 6 days before quenching into a water bath.

For Cr contents lower than 38.84 at%, non-reacted elemental Te/Se impurities were identified in the X-ray powder patterns and the unit cell parameters are very close to those of $Cr_{1.27}Q_2$. For Cr contents higher than 40.48 at%, compounds with the monoclinic $Cr_{3\pm x}Te_4$ structure type (space group: $I2/m$) were observed.

2.2. Chemical analysis

The compositions of the samples were determined by the ICP (Inductively Coupled Plasma) technique yielding $Cr_{1.27}Q_2/Cr_{5.08}Q_8$: $Cr_{1.270(12)}Q_2$, $Cr_{1.32}Q_2/Cr_{5.28}Q_8$: $Cr_{1.322(1)}Q_2$, and $Cr_{1.36}Q_2/Cr_{5.44}Q_8$: $Cr_{1.362(18)}Q_2$.

2.3. Powder X-ray diffraction and Rietveld refinement

X-ray powder patterns in the 2θ-range of 10–100° with sufficient statistics suitable for Rietveld refinements were collected on a STOE STADI P diffractometer in transmission geometry using Cu$K\alpha$ radiation ($\lambda = 1.54056$ Å) with a position sensitive detector. Rietveld refinements were done with the program package FULLPROF [11]. The background was interpolated by linear splines between selected points. The profiles of the reflections were modeled using a pseudo-Voigt function (3 parameters). Preferred orientation was treated using March's function. The atomic coordinates and isotropic displacement parameters B_{iso} were refined assuming a common parameter for the Te/Se atoms. For the $Cr_{(1+x)}Q_2$ phases, the position Cr1 is found to be fully and the Cr2 position is only partially occupied. Te and Se atoms are distributed statistically over the 2*d* site and the ratio of the Te:Se occupancy was fixed at 6:2. In total 13 structural parameters were refined. For the $Cr_{(5+x)}Q_8$ phases, the Cr2 and Cr3 positions are fully and the Cr1 and Cr4 positions are only partially occupied. Te and Se atoms are distributed statistically on the 2*d* and 6*i* sites. In total 21 structural parameters were varied. The refined parameters are listed in Table 1. Fig. 1 shows a plot of the final Rietveld refinement for $Cr_{5.44}Q_8$. Table 2 lists the atomic coordinates for two representative examples, $Cr_{1.27}Q_2$ and $Cr_{5.08}Q_8$. Selected interatomic distances are compiled in Table 3.

2.4. Magnetic measurements

The dc-magnetization measurements were performed with a MPMS SQUID magnetometer in the temperature range of $5\,K \leqslant T \leqslant 300\,K$ in a field of 0.01 and 1 T. Zero-field-cooled (ZFC) and field-cooled (FC) magnetization measurements (M_{ZFC} and M_{FC}) were done in the following way. The samples were cooled in zero field to 2 K, a field of 100 Oe was set immediately after $T = 2$ K was reached, and M_{ZFC} data were recorded upon warming from 2 to 300K; finally M_{FC} data were recorded on cooling from 300 K back to 2 K.

Table 1
Crystal data and structure refinement parameters of $Cr_{(1+x)}Q_2$ and $Cr_{(5+x)}Q_8$ (Q = Te, Se; Te:Se = 6:2)

Formula	$Cr_{(1+x)}Q_2$			$Cr_{(5+x)}Q_8$		
$(1+x)$ or $(5+x)$	1.27	1.32	1.36	5.08	5.28	5.44
Crystal system	Trigonal			Trigonal		
Space group	$P-3m1$			$P-3m1$		
a (Å)	3.8226(1)	3.8334(1)	3.8430(1)	7.6443(2)	7.6747(1)	7.6885(2)
c (Å)	5.9793(2)	6.0102(1)	6.0455(2)	11.9717(4)	12.0455(3)	12.1088(4)
V (Å^3)	75.664(2)	76.487(2)	77.322(2)	605.84(2)	614.44(2)	619.90(3)
Z	1			2		
2θ range (deg)	10–100			10–100		
N_{obs}	41	41	42	221	246	213
N_{ref}	13	13	13	21	21	21
R_{wp}	4.08	4.32	3.97	4.56	4.69	4.74
R_e	3.49	3.67	3.16	3.54	3.72	3.55
GOF/χ^2	1.37	1.39	1.58	1.66	1.59	1.79
DW	1.0732	1.0730	0.9130	0.9107	0.9471	0.8591
R_{Bragg}	4.76	5.13	5.40	3.99	5.16	3.97
R_F	4.67	5.81	6.90	8.67	9.66	9.43

Notes: The reliability factors values have the standard definitions. DW is the Durbin-Watson statistics.

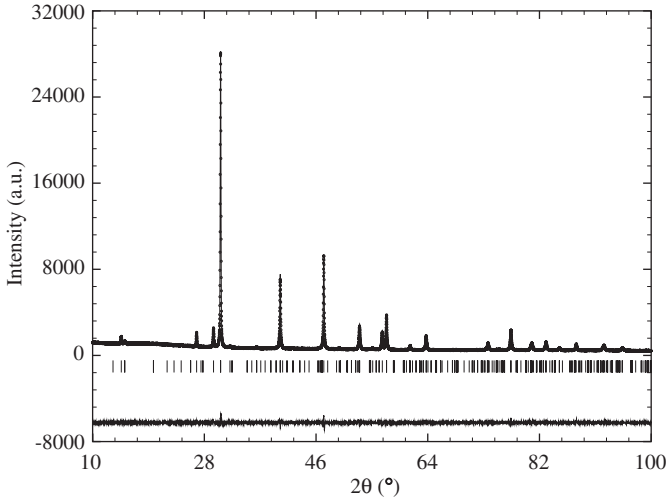

Fig. 1. Rietveld refinement plot for $Cr_{5.44}Q_8$ with peak markers and difference plot.

Table 2
Atomic coordinates for representative $Cr_{1.27}Q_2$ and $Cr_{5.08}Q_8$

Atom	Site	x	y	z	B_{iso}(Å^2)	sof
tr-$Cr_{1.27}Q_2$						
Cr1	1*a*	0	0	0	3.91(6)	1
Cr2	1*b*	0	0	0.5	3.91(6)	0.27
Te1	2*d*	3-Jan	3-Feb	0.2545(3)	2.44(2)	0.75
Se1	2*d*	3-Jan	3-Feb	0.2545(3)	2.44(2)	0.25
tr-$Cr_{5.08}Q_8$						
Cr1	1*b*	0	0	0.5	4.79(5)	0.576(12)
Cr2	6*i*	0.5022(6)	0.4978(6)	0.2515(13)	4.79(5)	1
Cr3	2*c*	0	0	0.2480(16)	4.79(5)	1
Cr4	3*e*	0	0.5	0	4.79(5)	0.528(12)
Te1	2*d*	3-Jan	3-Feb	0.3902(7)	3.56(2)	0.75
Te2	2*d*	3-Feb	3-Jan	0.1254(7)	3.56(2)	0.75
Te3	6*i*	0.1617(4)	0.8383(4)	0.1208(5)	3.56(2)	0.75
Te4	6*i*	0.8315(4)	0.1685(4)	0.3695(5)	3.56(2)	0.75
Se1	2*d*	3-Jan	3-Feb	0.3903(7)	3.56(2)	0.25
Se2	2*d*	3-Feb	3-Jan	0.1254(7)	3.56(2)	0.25
Se3	6*i*	0.1617(4)	0.8382(4)	0.1208(6)	3.56(2)	0.25
Se4	6*i*	0.8315(4)	0.1685(4)	0.3695(5)	3.56(2)	0.25

2.5. Differential scanning calorimetry

Differential scanning calorimetric experiments (DSC) were performed for $Cr_{5.44}Q_8$ using a thermal analyzer (Netzsch STA 449C) completely integrated into a glove box operated under argon ($p(O_2, H_2O) < 0.1$ ppm) to prevent hydrolysis and oxidation during sample preparation. A sample of 66.80 mg was loaded in a sealed niobium tube and the DSC data were collected between 293 and 1573 K. The heating and cooling rate was 10 K/min.

2.6. Theoretical investigations

The electronic structure of the $Cr_{(1+x)}Q_2$ system was calculated self-consistently using the spin polarized relativistic SPR-KKR method in the atomic sphere approximation (ASA) mode [12–15]. The details of the method have been described elsewhere [14,15]. Exchange and correlation effects were treated within the framework of local density functional theory, using the parametrization of Vosko et al. [16]. The CPA is used to describe the random distribution of Te/Se atoms within the chalcogen planes and the random distribution of the vacancies within the Cr layers [17,18]. Because of the rather large unit cell of the $Cr_{(5+x)}Q_8$ system we focused the calculations on the $Cr_{(1+x)}Q_2$ systems.

The effective exchange coupling parameters J_{ij} of a magnetically ordered system can be calculated among others on the basis of first order perturbation theory. A corresponding expression that was derived by Lichtenstein et al. [19] within the framework of the KKR formalism is used here. This approach has the great advantage that it

Table 3
Selected interatomic distances (Å) for $Cr_{(1+x)}Q_2$ and $Cr_{(5+x)}Q_8$

tr-$Cr_{1.27}Q_2$	tr-$Cr_{1.32}Q_2$	tr-$Cr_{1.36}Q_2$
Cr1–Cr1 3.8226(1)	Cr1–Cr1 3.8334(1)	Cr1–Cr1 3.8430(1)
Cr2–Cr2 3.8226(1)	Cr2–Cr2 3.8334(1)	Cr2–Cr2 3.8430(1)
Cr1–Cr2 2.9896(1)	Cr1–Cr2 3.0051(1)	Cr1–Cr2 3.0228(1)
Cr1–*Q*1 2.6807(10)	Cr1–*Q*1 2.6880(14)	Cr1–*Q*1 2.6966(10)
Cr2–*Q*1 2.6506(10)	Cr2–*Q*1 2.6623(13)	Cr2–*Q*1 2.6728(10)
tr-$Cr_{5.08}Q_8$	tr-$Cr_{5.28}Q_8$	tr-$Cr_{5.44}Q_8$
Cr2–Cr2 3.772(7)	Cr2–Cr2 3.579(6)	Cr2–Cr2 3.701(12)
3.873(7)	4.095(6)	3.987(12)
Cr3–Cr2 3.822(3)	Cr3–Cr2 3.842(3)	Cr3–Cr2 3.847(5)
Cr4–Cr4 3.8221(1)	Cr4–Cr4 3.8373(1)	Cr4–Cr4 3.8443(1)
Cr1–Cr3 3.017(19)	Cr1–Cr3 3.086(16)	Cr1–Cr3 3.078(18)
Cr2–Cr4 3.011(16)	Cr2–Cr4 3.061(11)	Cr2–Cr4 3.085(12)
Cr1–*Q*4 6 × 2.724(4)	Cr1–*Q*4 6 × 2.704(3)	Cr1–*Q*4 6 × 2.722(6)
Cr2–*Q*1 1 × 2.785(11)	Cr2–*Q*1 1 × 2.620(9)	Cr2–*Q*1 1 × 2.648(12)
Cr2–*Q*2 1 × 2.650(11)	Cr2–*Q*2 1 × 2.831(9)	Cr2–*Q*2 1 × 2.790(12)
Cr2–*Q*3 2 × 2.744(10)	Cr2–*Q*3 2 × 2.676(8)	Cr2–*Q*3 2 × 2.705(11)
Cr2–*Q*4 2 × 2.598(10)	Cr2–*Q*4 2 × 2.685(7)	Cr2–*Q*4 2 × 2.656(11)
Average 2.687	Average 2.696	Average 2.693
Cr3–*Q*3 3 × 2.627(12)	Cr3–*Q*3 3 × 2.637(9)	Cr3–*Q*3 3 × 2.658(12)
Cr3–*Q*4 3 × 2.663(11)	Cr3–*Q*4 3 × 2.645(9)	Cr3–*Q*4 3 × 2.670(12)
Average 2.645	Average 2.640	Average 2.640
Cr4–*Q*2 2 × 2.669(5)	Cr4–*Q*2 2 × 2.676(5)	Cr4–*Q*2 2 × 2.676(5)
Cr4–*Q*3 4 × 2.667(4)	Cr4–*Q*3 4 × 2.670(3)	Cr4–*Q*3 4 × 2.670(3)
Average 2.668	Average 2.672	Average 2.664

can be applied to disordered or substoichiometric systems as well. Performing a Fourier transformation for the resulting exchange coupling constants leads to the magnon dispersion relation $E(q)$. This in turn can be used in combination with the random phase approximation (RPA) Green's function approach [20] to determine the critical temperature of the system. Because this approach assumes an ordered system it is not immediately applicable to the substoichiometric systems considered here. For that reason the so-called virtual crystal approximation has been applied that replaces the incompletely occupied Cr sublattice (see below) by a fully occupied one with the exchange coupling parameter scaled down according to the occupation number.

A more detailed insight into the magnetic properties at finite temperatures has been obtained by performing Monte Carlo (MC) simulations. The results presented below have been obtained on the basis of a classical Heisenberg Hamiltonian using the calculated exchange coupling constants. The MC simulation to study the temperature dependence of the magnetization has been performed by cooling gradually the alloy system from a high temperature (cooling simulation). A lattice of $6 \times 6 \times 6$ cells with periodic boundary conditions has been used. In the present investigations we use a simplified model and consider only the interactions between the Cr magnetic moments, taking into account only the nearest and next-nearest neighbor interactions for Cr atoms. Corresponding simulations for the cooling curves of $Cr_{1.27}Q_2$ have been made without (ZFC) and with (FC) an external magnetic field included in the underlying Hamiltonian.

3. Results and discussion

3.1. Crystal structures

The crystal structure parameters of the high temperature phases $Cr_{(1+x)}Q_2$ and low temperature phases $Cr_{(5+x)}Q_8$ as obtained from the Rietveld refinements of X-ray powder diffraction patterns (see Fig. 1) are compiled in Table 1. Compared to the patterns of $Cr_{(1+x)}Q_2$, the powder diffraction patterns of $Cr_{(5+x)}Q_8$ revealed weak additional reflections which could be indexed on the basis of a trigonal supercell with all cell parameters being doubled. The additional reflections are weak indicating the close structural relationship of the phases, but they were always clearly seen (see Fig. 2) and allowed to distinguish the two phases.

With increasing Cr content the trigonal cell parameter a and c in both series increase in a linear fashion (Fig. 3). For the phases with the trigonal basic cell, the a and c parameters change from 3.8226, 5.9793 to 3.8430, 6.0455 Å; while for phases with the supercell, the a, c axes increase from 7.6743, 11.9717 to 7.6885, 12.1088 Å. The increase of the c lattice parameter is about two times of that of the a-axis, implying that the expansion along the c direction is more significant than within the ab plane. Compared with $Cr_{(1+x)}Q_2$ (Q = Te/Se; Te:Se = 7:1) [9], the a and c parameters for $Cr_{(1+x)}Q_2$ with Te:Se = 6:2 are smaller. For example, the a and c lattice parameters for $Cr_{1.264}Q_2$ (Te:Se = 7:1) [9] are 3.8740 and 6.0179 Å,

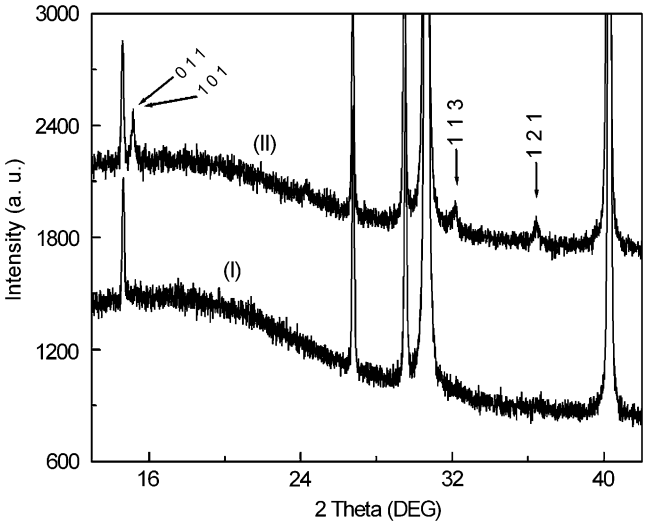

Fig. 2. Local XRD patterns for a trigonal basic cell (I) and trigonal supercell (II).

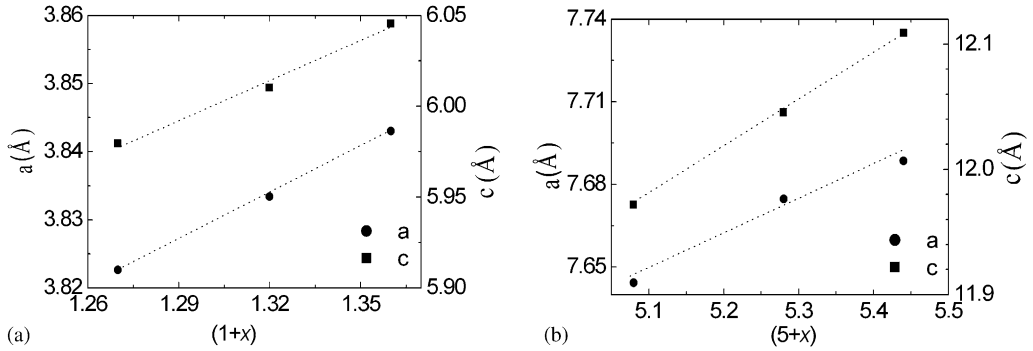

Fig. 3. Dependences of cell parameters on chromium content in $Cr_{(1+x)}Q_2$ (a) and $Cr_{(5+x)}Q_8$ (b). Dotted lines are used as guides for the eyes.

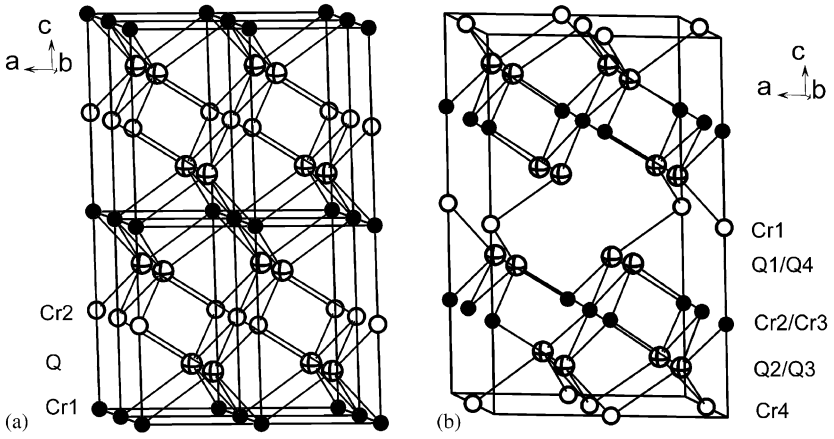

Fig. 4. Crystal structures of trigonal $Cr_{(1+x)}Q_2$ with basic cell (a) and trigonal $Cr_{(5+x)}Q_8$ with supercell (b).

respectively, whereas for $Cr_{1.27}Q_2$ (Te:Se = 6:2) they are 3.8226 and 5.9793 Å indicating that a higher Se content in $Cr_5Te_{8-y}Se_y$ leads to a contraction of the unit cell parameters.

Plots of the crystal structures of trigonal $Cr_{(1+x)}Q_2$ and $Cr_{(5+x)}Q_8$ are presented in Fig. 4. The structures can be viewed as a variant of the hexagonal NiAs-type structure but with additional metal atom vacancies. The Q atoms are hexagonal close packed and the Cr atoms occupy the octahedral interstices. Thus, completely filled and deficient metal atom layers are stacked alternatively along the c-axis.

Within the layers, CrQ_6 octahedra share common edges, while CrQ_6 octahedra in neighbored layers have common faces and relatively short Cr–Cr separations along the crystallographic c-axis result. The shortest Cr–Cr distances, ranging from 2.99 to 3.02 Å for the $Cr_{(1+x)}Q_2$ phases and from 3.01 to 3.09 Å for the $Cr_{(5+x)}Q_8$ phases, respectively, are listed in Table 3. Such short Cr–Cr distances allow weak bonding interactions between these metal centers. The partial occupancy of metal atom sites in the deficient layers prevents the formation of infinite Cr–Cr atom chains along the c-axis.

An interesting feature of these structures is the differences of Cr–Q distances in the completely filled and in the deficient metal atom layers. In the $Cr_{(1+x)}Q_2$ phases, the CrQ_6 octahedra are nearly regular (Table 3). The Cr1–Q1 distances range from 2.6807 to 2.6966 Å within the completely filled metal layers and from 2.6506 to 2.6726 Å within the deficient metal layers. For the $Cr_{(5+x)}Q_8$ phases, the CrQ_6 octahedra are markedly distorted and especially the angles around Cr2/Cr3 significantly deviate from ideal values. In addition, the Cr2–Q bond lengths scatter between 2.598(10) and 2.785(11) Å for $Cr_{5.08}Q_8$ and from 2.648(12) to 2.790(12) Å for $Cr_{5.44}Q_8$ (Table 3). In the phases that crystallize in the supercell, the distortion of CrQ_6 octahedra and the existence of the torsion in the Cr substructure seem to weaken the coupling of magnetic moments and affect the magnetic properties.

The transition from the $Cr_{(5+x)}Q_8$ phases exhibiting the supercell to the phases $Cr_{(1+x)}Q_2$ was studied by differential scanning calorimetry. An example for a compound with the trigonal supercell ($Cr_{5.44}Q_8$) is presented in Fig. 5. A sharp peak at 1524 K is assigned as the melting point of $Cr_{5.44}Q_8$, and the broad shoulder before this peak may be caused by the transition from the trigonal supercell to the trigonal basic cell. The shoulder starts at about 1063 K and it is ascribed to an endothermic vacancy order–disorder transition. The reversibility of the transition is confirmed by the cooling curve of the DSC shown in the inset of Fig. 5. In addition, the reversibility was further confirmed by identifying the high temperature or low temperature

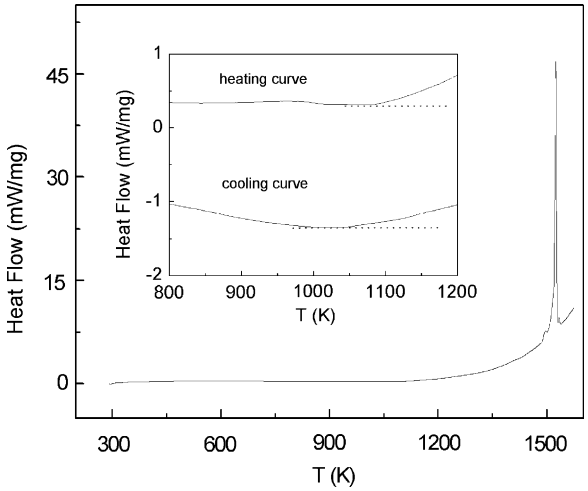

Fig. 5. DSC trace of $Cr_{5.44}Q_8$ sealed in a Nb tube with a heating rate 10 °C/min. The inset is the enlarged one between 800 and 1200 K. Dotted lines are used as guides for the eyes.

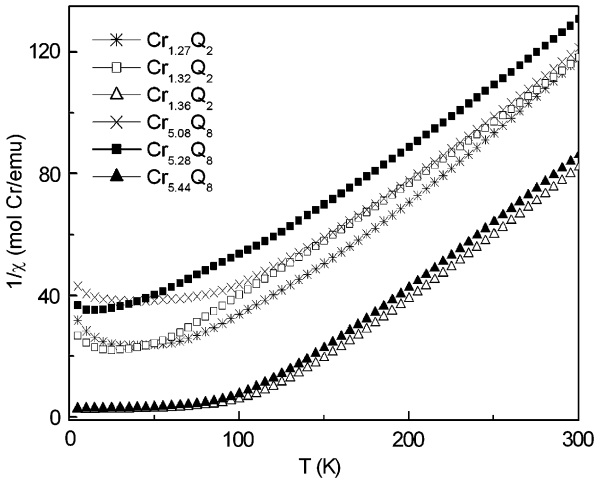

Fig. 6. Temperature dependencies of the inverse magnetic susceptibility of $Cr_{(1+x)}Q_2$ and $Cr_{(5+x)}Q_8$ at field of 1 T.

phases by annealing the sample above or below 1063 K, respectively, for several cycles, with quenching mode and by powder X-ray diffraction. This transition originates from the intralayer disordering of metal vacancies in the alternating partially filled metal layers. Similar order–disorder phenomena occurring at elevated temperatures were reported for Cr_3Te_4 and Cr_5Te_8 [3g,h].

The substitution of two Te atoms by two Se atoms in Cr_5Te_8 has led to the formation of the high temperature $Cr_{(1+x)}Q_2$ phases with a trigonal basic cell and low temperature $Cr_{(5+x)}Q_8$ phases with a trigonal supercell. Such substitution invokes changes of the magnetic interactions. The disorder of the Cr atoms in the metal deficient layers, and the random distribution of Te and Se atoms in the anion layers may generate magnetic frustration, thus introducing spin-glass or cluster-glass behavior in these materials as will be discussed below.

3.2. Magnetic properties

The temperature dependence of the inverse magnetic susceptibilities for $Cr_{(1+x)}Q_2$ ($(1+x) = 1.27$, 1.32, 1.36) and $Cr_{(5+x)}Q_8$ ($(5+x) = 5.08$, 5.28, and 5.44) ($H = 1$ T) are plotted in Fig. 6. In all cases, $\chi(T)$ obeys the Curie–Weiss law $\chi(T) = C/(T-\theta_P)$ in the temperature range of 200–300 K. Note that the data are not corrected for the paramagnetic contribution of the conducting electrons and the diamagnetic contributions from closed shells. The evaluated effective magnetic moment μ_{eff} and the paramagnetic Curie temperature θ_P are listed in Table 4. The values for μ_{eff} are between 4.10 and 4.40 μ_B per Cr atom, slightly larger than the expected spin-only moment of 3.87 μ_B for Cr^{3+}. In the temperature region between 300 and 600 K the magnetic moments per Cr atom are still larger than the spin-only value and amount to about 4.15 μ_B for the different compounds. Such a high value for μ_{eff} is quite unusual for Cr^{3+}, but was often observed for chromium chalcogenides [21]. It may be due to an electron transfer from Q to Cr via d–p hybridization [22]. In an ionic picture the coexistence of Cr^{3+} (d^3) and Cr^{4+} (d^2) is required for the two compounds with the lowest Cr content, and Cr^{3+} and Cr^{2+} (d^4) should coexist in the two Cr rich phases. In the former cases the effective magnetic moment should be slightly smaller than 3.87 μ_B, and for the Cr rich samples a larger magnetic moment is expected.

Table 4
Magnetic characteristics for $Cr_{(1+x)}Q_2$ and $Cr_{(5+x)}Q_8$

$1+x$ or $5+x$	μ_{eff},[a] [μ_B/Cr]	θ_p[a] [K]	H[a] [T]	T_{min}/T_{max}[a] [K]	T_c [K]	T_f [K]
1.27	4.10	53	1	200/300	64	58
1.32	4.40	15	1	200/300	56	48
1.36	4.30	111	1	200/300	82	63
5.08	4.27	24	1	200/300	—[b]	—[b]
5.28	4.35	−9	1	200/300	16	—[b]
5.44	4.28	103	1	200/300	72	58

[a] μ_{eff} and θ_p are the results of fits of Curie–Weiss law to the magnetic susceptibilities. H is the applied field. T_{min}/T_{max} indicate the range of the fit.

[b] The values are not well defined.

The paramagnetic Curie temperatures are quite large and positive for $Cr_{1.36}Q_2$ (111 K) and $Cr_{5.44}Q_8$ (103 K), indicating strong predominant ferromagnetic exchange interactions. For $Cr_{1.27}Q_2$ (53 K) and $Cr_{5.08}Q_8$ (24 K) the values are lower, and they are small positive or negative for $Cr_{1.32}Q_2$ (15 K) and $Cr_{5.28}Q_8$ (−9 K).

In order to characterize the magnetic behavior of these compounds at low temperatures, the temperature dependence of ZFC/FC magnetization was measured. Fig. 7 shows the M_{ZFC} and M_{FC} curves for $Cr_{(1+x)}Q_2$ and $Cr_{(5+x)}Q_8$.

Several observations should be shortly highlighted: (a) a thermal irreversibility for the ZFC/FC magnetization exists for all samples below a freezing temperature T_f; (b) for the

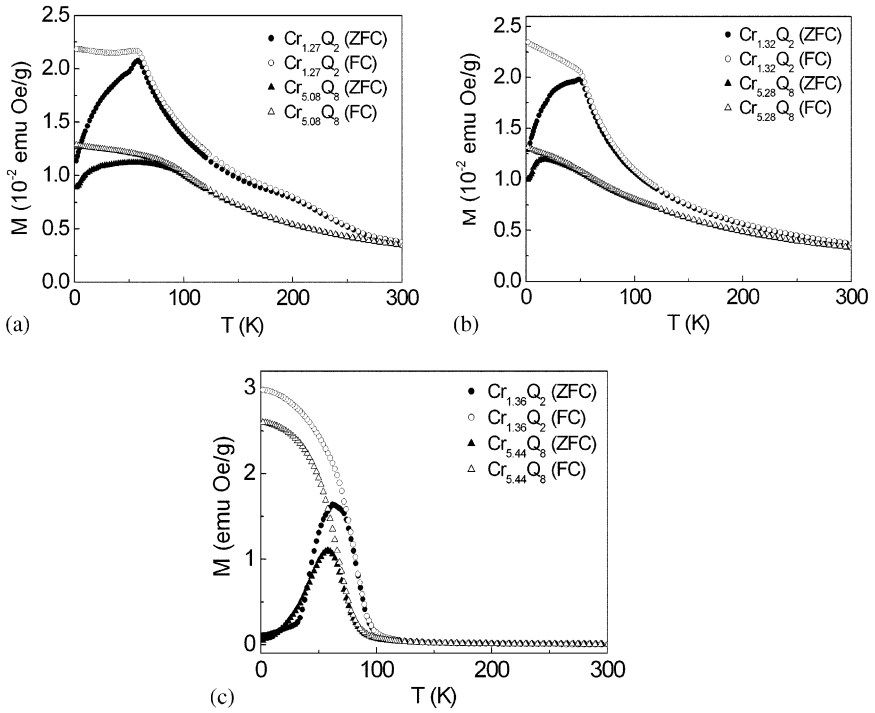

Fig. 7. Temperature-dependent M_{ZFC} and M_{FC} with $H = 100$ Oe for (a) $Cr_{1.27}Q_2$ and $Cr_{5.08}Q_8$, (b) $Cr_{1.32}Q_2$ and $Cr_{5.28}Q_8$, and (c) $Cr_{1.36}Q_2$ and $Cr_{5.44}Q_8$.

same Cr/Q ratio, the phases with trigonal basic cells show a stronger magnetization and have higher T_c and T_f values (Table 4, T_c and T_f as defined in Refs. [9,10]) than the phases with trigonal supercells; (c) for the same structure type, basic cell or supercell, $Cr_{1.36}Q_2$ and $Cr_{5.44}Q_8$ with the highest Cr content show the strongest magnetization and have the highest values for T_c and T_f. The other two series, $Cr_{1.27}Q_2/Cr_{5.08}Q_8$ and $Cr_{1.32}Q_2/Cr_{5.28}Q_8$, have a similar magnitude of magnetization with lower T_f values for the $Cr_{1.32}Q_2/Cr_{5.28}Q_8$ series.

Fig. 7a shows the magnetization curves M_{ZFC} and M_{FC} for $Cr_{1.27}Q_2$ and $Cr_{5.08}Q_8$ that are characteristic for spin-glass behavior. The FC trace is almost flat below the freezing temperature [23]. A sharp freezing temperature T_f of 58 K is seen for $Cr_{1.27}Q_2$. In contrast, for $Cr_{5.08}Q_8$ the freezing regime is broadened and the freezing temperature is less well defined. In addition, a small hump around 200 K is observed in both the FC and ZFC curves of $Cr_{1.27}Q_2$, which we tentatively interpret as spin reorientation processes.

The magnetization curves for $Cr_{1.32}Q_2$ and $Cr_{5.28}Q_8$ (Fig. 7b) show a small difference compared with that of $Cr_{1.27}Q_2$ and $Cr_{5.08}Q_8$. The FC trace exhibits a small increase below the freezing temperature of 48 K for $Cr_{1.32}Q_2$. For $Cr_{5.28}Q_8$ the value for T_f is not well defined. Considering the small magnitude of the FC magnetization, we describe such phenomenon as spin-glass or spin-glass-like behavior.

The magnetization M_{ZFC} and M_{FC} for $Cr_{1.36}Q_2$ and $Cr_{5.44}Q_8$ is shown in Fig. 7c. The curves are completely different from those in Fig. 7a and b with respect to the magnitude of the magnetization and the temperature dependence. The ZFC magnetization curve displays a broad maximum at 63 K for $Cr_{1.36}Q_2$ and at 58 K for $Cr_{5.44}Q_8$, and in the FC curve a sharp and continuous increase with decreasing temperature occurs below T_c.

Such a behavior is different from that of typical spin-glass behavior and rather resembles that of a ferri- or ferromagnet with the broad maximum in the FC traces originating from domain re-orientations as the temperature approaches the transition temperature from below.

In a previous investigation we reported the effect of anion and cation substitution in Cr_5Te_8 [9,10]. We characterized the phases $Cr_{(1+x)}Q_2$ (Q = Te, Se, Te:Se = 7:1) and $Cr_4Ti_1Te_8$ which crystallize with trigonal basic cells and in a monoclinic system, respectively. They show very similar magnetization irreversibilities as described above. A similar splitting of FC and ZFC magnetization curves has recently been reported and was interpreted as cluster-glass properties (CG) for the following materials: $La_{0.7}Sr_{0.3}Mn_{0.7}Co_{0.3}O_3$ [24(a)], $La_{0.5}Sr_{0.5}CoO_3$ [24(b), (c)], $Fe_{1/3}TiS_2$ [24(d)], $Ca_{0.9}Sm_{0.1}MnO_3$ [24(e)], and the molecular-based magnet $K_{1-2x}Co_{1+x}[Fe(CN)_6]\cdot yH_2O$ [24(f), (g)]. The rapid rise of the magnetization around T_c observed for $Cr_{1.36}Q_2$ and $Cr_{5.44}Q_8$ may be associated with the occurrence of finite range ferromagnetic ordering, forming spin clusters near the critical temperature, and the clusters are randomly frozen as T is further decreased. A 'quasi'-critical temperature or Curie temperature T_c and a freezing temperature T_f may be defined like in [9,10] as the temperatures where the minimum of $d\chi_{(ZFC)}/dT$ occurs and where $d\chi_{(ZFC)}/dT$ intersects zero. Using the Curie

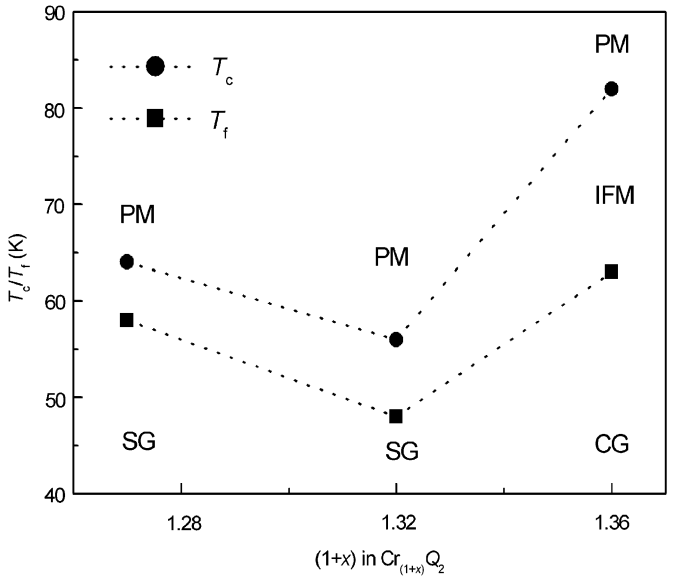

Fig. 8. Tentative magnetic phase diagram for $Cr_{(1+x)}Q_2$. Dotted lines are guides to the eye. PM: paramagnetism; SG: spin-glass; CG: cluster-glass; IFM: intra-cluster ferromagnetism or short-ranged FM ordering, i. e. the formation of clusters.

temperature T_c and the freezing temperature T_f, a tentative magnetic phase diagram may be suggested for the $Cr_{(1+x)}Q_2$ series (Fig. 8). It reveals that the lowest values for T_c and T_f are observed for the $Cr_{1.32}Q_2$ phases (Table 4). In the low temperature region spin- and cluster-glass properties occur for low and high Cr contents, respectively. This finding may be related to the ratio of the number of Cr atoms distributed over the vacancies and their specific local distribution patterns in the metal-deficient layers.

Another important remark is about the comparison with the results of our former study of $Cr_{(1+x)}Q_2$ (Q = Te, Se; Te:Se = 7:1) [9]. In general, for the same Cr:Q ratio the phases of the 7:1 series exhibit a stronger magnetization and have higher values for T_c and T_f.

In order to explain the observed magnetic properties, the following chemical, structural, and magnetic exchange mechanisms have to be taken into consideration:

(i) A continuous increase of the concentration of Cr by changing the ratio of Cr:Q, i.e. the number of magnetic moments per unit volume should lead to a continuous variation of the transition temperatures. However, a minimum is found for the $Cr_{1.32}Q_2/Cr_{5.28}Q_8$ phases and its origin will be explored in the next section.

(ii) The ratio of Te:Se: a higher Se content in $Cr_{5\pm x}Te_{8-y}Se_y$ shortens the Cr–Cr separation thus increasing antiferromagnetic exchange interactions and leads to a decreasing magnitude of magnetization, the Curie temperature, and the freezing temperature.

(iii) In the phases crystallizing with supercells, the distortion of CrQ_6 octahedra in the completely filled metal atom layers, and the dislocation of Cr1 and Cr4 in the metal atom deficient layers weaken the magnetic interactions, thus resulting in a reduced magnetization and lower values for T_c and T_f compared to the system with trigonal basic cells.

(iv) The structural disorder implies a random distribution of Te and Se atoms in the anion layers and the disorder of Cr atoms in the metal atom deficient layers (Cr2 in the basic cell and Cr1 and Cr4 in the supercell). Structural disorder induces magnetic disorder, and competition of ferromagnetic and antiferromagnetic interactions through Cr–Te–Cr, Cr–Se–Cr bridges and Cr–Cr interactions may lead to a frustration.

In summary, the coexistence of disorder and frustration thus induces a gradual shift from a ferromagnetic re-entrant spin-glass observed for m-Cr_5Te_8 [10] to a cluster-glass behavior in the $Cr_{5+x}Te_7Se$ series [9] to spin-glass and cluster-glass properties in the $Cr_{5+x}Te_6Se_2$ series.

3.3. Band-structure calculations

The electronic band structure of Cr chalcogen compounds is dominated in the valence band regime by the exchange-split *d*-bands of the Cr-atoms that hybridize with the chalcogen *p*-states. The semi-core band at lower binding energy on the other hand, originate primarily from chalcogen *s*-states. Fig. 9 shows the corresponding results for $Cr_{1.27}Q_2$ (with $Q = Te_{0.75}Se_{0.25}$ in the following) obtained for the energetically favored antiferromagnetically ordered configuration with the magnetic moments on the sites Cr1 and Cr2 being antiparallel. While panel Fig. 9(a) shows the spin and component resolved contributions together with the total DOS, in Fig. 9(b) and (c) the spin-resolved *d*-like DOS for sites Cr1 and Cr2 are separately displayed. In addition to the results for AFM $Cr_{1.27}Q_2$, corresponding DOS curves for ordered CrQ have been added in Fig. 9(b) and (c) (dashed lines). This reference compound shows preferential ferromagnetic (FM) order with the two Cr sites being equivalent. Obviously, the incomplete occupation of the Cr2 sites in $Cr_{1.27}Q_2$ leads—compared to the ordered compound CrQ—to a change from FM to AFM ordering. In addition one notes a broadening and smearing of the d-like DOS on the Cr2 sites of $Cr_{1.27}Q_2$ in Fig. 9 due to the random occupation of this sub-lattice.

The DOS curves in Fig. 9 clearly demonstrate that the electronic structure of $Cr_{(1+x)}Q_2$ depends very sensitively on the magnetic ordering and on the composition. In addition there will be a dependency on the occupation of the two nonequivalent Cr sites for the substoichiometric compounds. Our previous experimental and theoretical investigations had already indicated that a complete occupation of site Cr1 and an incomplete for site Cr2 is favored compared to the situation with both sites being occupied to the same extent. This finding was confirmed within the present work. Moving Cr1 atoms to site Cr2 leads to a monotonous increase of the energy until both lattice sites are equally occupied (Fig. 10). It is obvious

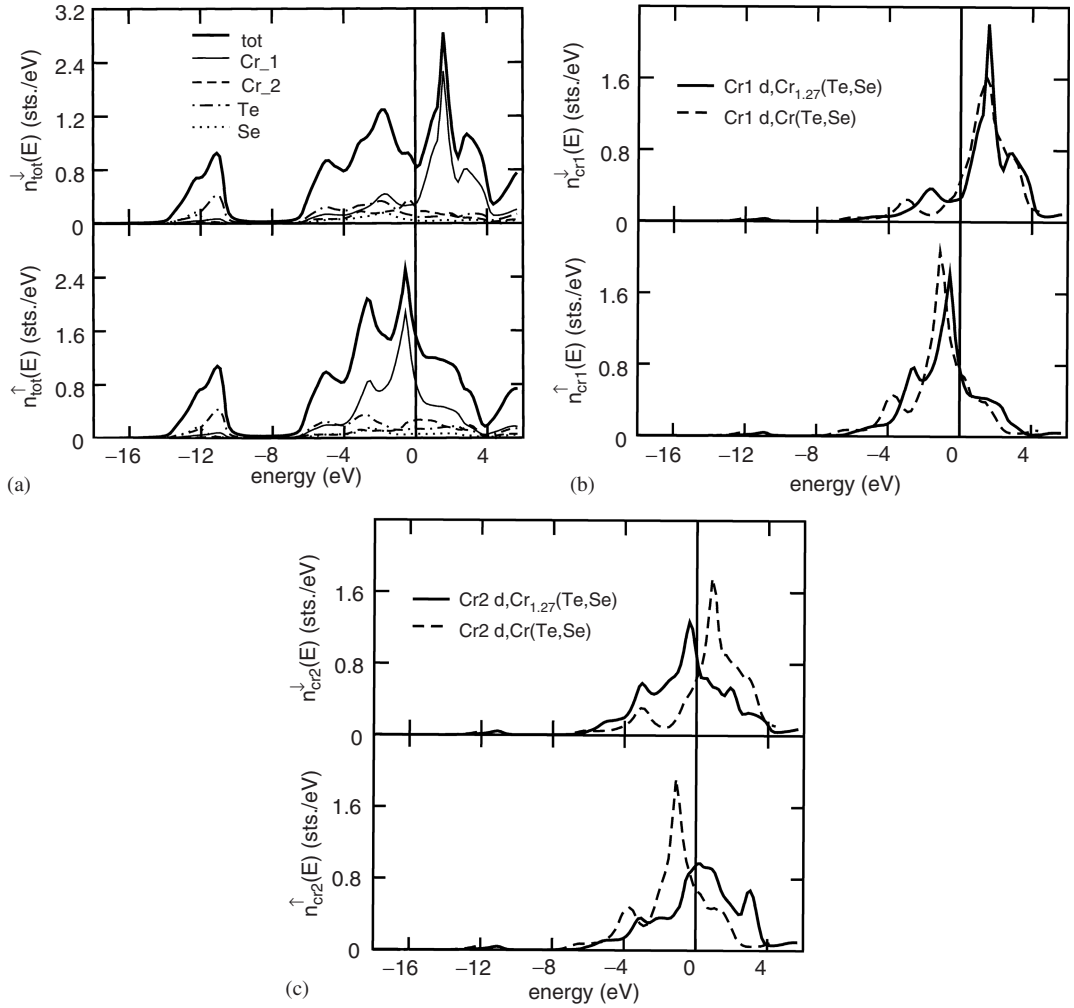

Fig. 9. DOS of the $Cr_{1.27}Q_2$ and CrQ phases obtained from the SPR-KKR calculations: (a) spin and component resolved contributions together with the total DOS of $Cr_{1.27}Q_2$; (b) and (c) the spin-resolved d-like DOS for sites Cr1 and Cr2, respectively. The origin of the energy scale corresponds to the Fermi energy.

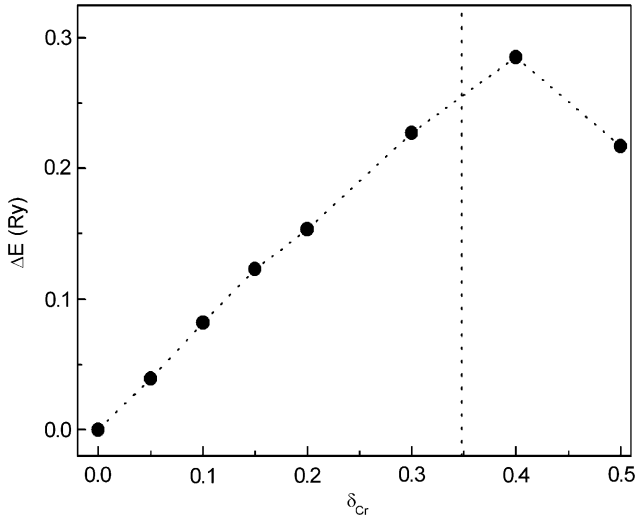

Fig. 10. Variation of the total energy of $Cr_{1.27}Q_2$ as a function of δ_{Cr} of Cr atoms moved from site Cr1 to site Cr2. $\delta_{Cr}=0$ corresponds to a complete occupation of site Cr1, while $\delta_{Cr}=0.365$ corresponds to an equal occupation of both sites. Dotted lines are used as guides for the eyes.

from Fig. 10 that the energy curve is not perfectly symmetric around the transfer value of $\delta_{Cr}=0.365$ Cr atoms. This is due to the lattice distortions with respect to the perfect NiAs structure that was kept fixed within the present study. The result that site Cr1 should be completely occupied and the remaining Cr atoms should occupy site Cr2, applies also for the other Cr concentrations considered here.

Apart from the site occupation also the lattice parameters and atomic coordinates within the unit cell can in principle be determined theoretically. Because of the large computational efforts connected with an optimization of all these parameters, total energy calculations have been performed for $Cr_{(1+x)}Q_2$ only in order to optimize the lattice parameters a while keeping the experimental values of the c/a ratio constant. The lattice parameters corresponding to the minimum of the total energy are plotted in Fig. 11. They increase with increasing Cr concentration, which is in accordance with the experimental findings. However, as found in many LSDA-based studies the

theoretical lattice parameters turned out to be about 2.7% too low compared with the experimental values. Applying the parametrization of the exchange correlation potential on the basis of the general gradient approximation (GGA) [25] should remove this shortcoming of the LSDA approach.

The magnetic moments of the various nonequivalent atoms in $Cr_{(1+x)}Q_2$ obtained for the optimized magnetic configuration, the site occupation and lattice parameter a are given in the first 3 columns of Table 5. We note that the absolute value of the Cr local magnetic moment increases with the Cr concentration. However, in the partially occupied Cr layer this increase is essentially more pronounced. Inspecting the change of the induced magnetic moments of Te and Se, the simultaneous decrease of their absolute values is recognized. These concentration dependent changes of local magnetic moments are related to the change in the hybridization of Te and Se p-states with the Cr d-states of the two adjacent nonequivalent Cr layers. Obviously, with increasing Cr concentration x the various moments approach values corresponding to the ideal antiferromagnetic configuration of the NiAs structure. However, as demonstrated by the results for CrQ given in column 4 of Table 5 and obtained for the antiferromagnetic configuration, the ideal spin-compensated configuration is not reached because of lattice distortions described above. Column 5 (Table 5) gives corresponding results for CrQ obtained for the ferromagnetic configuration. With respect to the AFM configuration, it is primarily the moment of Cr2 atoms that changes the sign and increases in magnitude. The influence of the lattice parameters is demonstrated by the results listed in column 7 (Table 5). As may be expected, an increase of the lattice parameters leads to an increase of the magnetic moments.

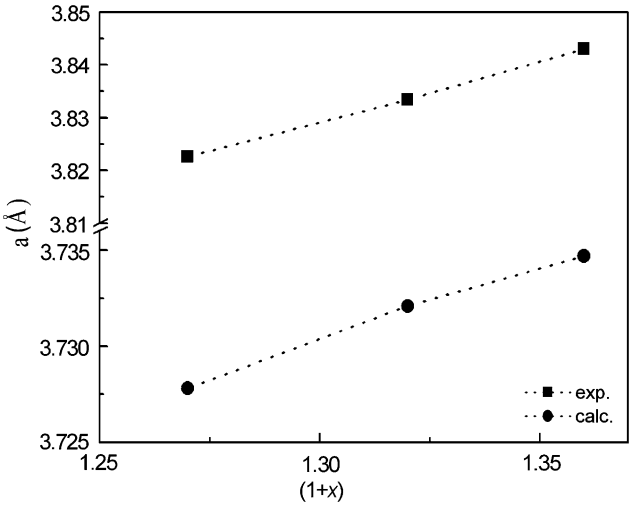

Fig. 11. The lattice parameters a of $Cr_{(1+x)}Q_2$ with $(1+x) = 1.27$, 1.32 and 1.36 calculated for a fixed c/a ratio in comparison with experiment. Dotted lines are used as guides for the eyes.

Table 5
Calculated magnetic moments (μ_B) in $Cr_{(1+x)}(Te_{0.75}Se_{0.25})_2$

	$x = 0.27$	$x = 0.32$	$x = 0.36$	CrQ ($a_{x=0.27}$, AFM)	CrQ ($a_{x=0.27}$, FM)	CrQ (FM)
Cr1	2.732	2.782	2.809	2.746	2.746	3.057
Cr2	−1.283	−1.451	−1.502	−2.247	2.318	2.656
Te	−0.130	−0.122	−0.113	0.006	−0.018	−0.030
Se	−0.188	−0.177	−0.166	0.003	−0.013	−0.032

The results presented in Table 5 correspond to ideal collinear spin-configurations with the magnetic moments located on sites Cr1 and Cr2 being either parallel (FM) or antiparallel. In spite of this restriction they nevertheless supply a suitable reference system to deal with the complex spin configurations and the finite temperature magnetism of Cr chalcogen compounds. This is achieved by calculation of the effective exchange coupling constants J_{ij}. The corresponding calculations have been performed for the equilibrium lattice parameters, i.e. those corresponding to the minimum of the total energy. The Cr1–Cr1, Cr2–Cr2 and Cr1–Cr2 exchange coupling constants for the alloys with $(1+x) = 1.27$, 1.32, 1.36 are compared in Fig. 12. The largest concentration dependence is observed for the interactions with the first and second neighboring Cr atoms. In addition, a non-monotonic change of the exchange coupling parameters between certain atoms occurs when the concentration of Cr increases (Fig. 12). We believe that this is the main reason for the experimentally observed non-monotonic concentration dependence

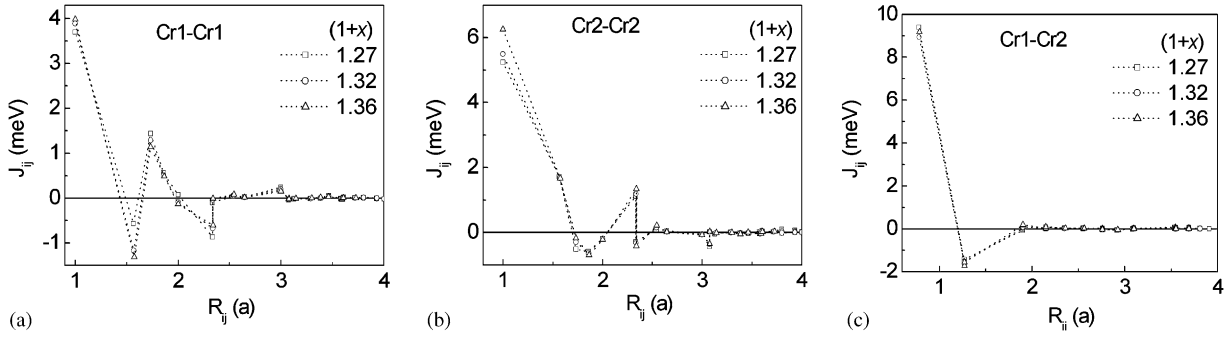

Fig. 12. Theoretical exchange coupling constants for $Cr_{(1+x)}Q_2$ with $(1+x) = 1.27$, 1.32 and 1.36 for (a) Cr1–Cr1, (b) Cr2–Cr2 and (c) Cr1–Cr2 atom pairs. Dotted lines are used as guides for the eyes.

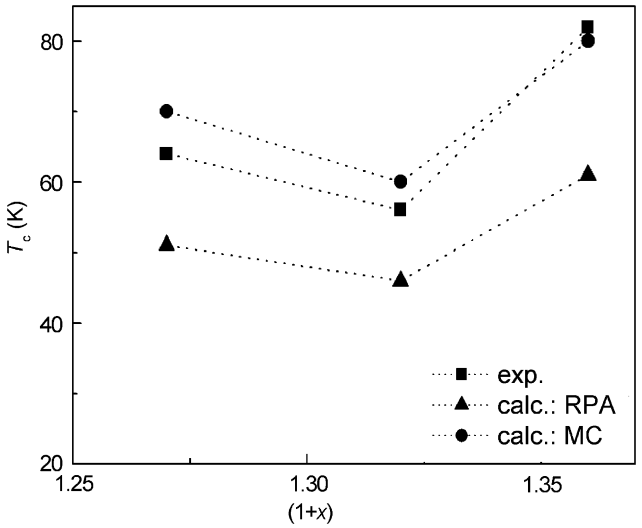

Fig. 13. Critical temperature T_c of $Cr_{(1+x)}Q_2$ for $(1+x) = 1.27$, 1.32 and 1.36 calculated via the RPA-method and Monte Carlo simulations in comparison with the corresponding experimental data. Dotted lines are used as guides for the eyes.

of the calculated Curie temperature discussed in detail below. Adopting the virtual crystal model and performing a Fourier transform of the exchange coupling constants J_{ij} rescaled according to the corresponding concentration allows determining the critical temperature T_c on the basis of the RPA method. The results obtained for $Cr_{(1+x)}Q_2$ for various concentrations are displayed in Fig. 13. Although the numerical results fall somewhat below the experimental data, they nevertheless reproduce the concentration dependence of T_c quite well. As already mentioned above, this variation of T_c with concentration x seems to be caused by the non-monotonous dependence of the exchange coupling constants J_{ij} on x. In addition to the application of the RPA method, the critical temperature T_c has been determined by means of Monte Carlo simulations as described above. The results obtained by this way are shown in Fig. 13 and reproduce the experimental data quite well. Again the variation with concentration has to be ascribed to that of the exchange coupling constants.

4. Conclusion

Different sample preparation conditions yield pure $Cr_{(1+x)}Q_2$ phases with a trigonal basic unit cell and pure $Cr_{(5+x)}Q_8$ phases with a trigonal supercell with Cr contents ranging from 38.84 to 40.48 at%. The substitution of two Te by two Se atoms in Cr_5Te_8 leads to a further decrease of T_c, compared to the previously studied Cr_5Te_7Se substitution system. Increasing the number of Se atoms implies more antiferromagnetic interaction paths via the Se bridges and shorter Cr–Cr distances, thus introducing more magnetic frustration into the 3D lattice. The ferromagnetic re-entrant spin-glass Cr_5Te_8 thus changes its character first to a cluster-glass behavior in the Cr_5Te_7Se system, and then to spin-glass and cluster-glass behavior in the $Cr_5Te_6Se_2$ system, depending on the Cr content and structure type.

Accompanying SPR-KKR-CPA band structure calculations give detailed insight into the electronic structure of the $Cr_{(1+x)}Q_2$ phase. This includes related ground state properties as well as equilibrium lattice parameters, site occupation and magnetic ordering. Subsequent Monte Carlo simulations on the basis of the calculated exchange coupling constants reproduce the experimental critical temperature T_c in a very satisfying way. In particular, the concentration dependence of T_c could be traced back to the concentration dependence of the coupling constants. Corresponding investigations on the computationally more demanding $Cr_{(5+x)}Q_8$ phases are in progress.

Studies of compounds with a higher degree of Se substitution are in progress. Our recent neutron TOF diffraction studies show the coexistence of FM and AFM long-range order at low temperatures for both m-Cr_5Te_8 and m-$Cr_4Ti_1Te_8$, and only short-range order for m-$Cr_{3.5}Ti_{1.5}Te_8$ and tr-$Cr_3Ti_2Te_8$. They will be reported in forthcoming publications. Neutron scattering experiments are scheduled to determine the magnetic structures and the Te/Se atom distribution.

Acknowledgments

The authors thank Ms. Eva Brücher (MPI Stuttgart) for her help in magnetic measurements, Dr. Rainer Niewa (MPI Dresden) for DSC experiments and Mr. H. Hartl (LMU-Munich) for chemical analysis (ICP). The DFG is acknowledged for the financial support of SPP 1136 project (BE 1653/12-2).

References

[1] (a) J. Dijkstra, C.F. Van Bruggen, C. Haas, R.A. de Groot, Phys. Rev. B 40 (1989) 7973–7976;
(b) M.S. Park, S.K. Kwon, S.J. Youn, B.I. Min, Phys. Rev. B 59 (1999) 10018–10024;
(c) W.H. Xie, Y.Q. Xu, B.G. Liu, D.G. Pettifor, Phys. Rev. Lett. 91 (2003) 037204-1–037204-4;
(d) W.H. Xie, B.G. Liu, D.G. Pettifor, Phys. Rev. B 68 (2003) 134407-1–134407-7.
[2] (a) H. Haraldsen, E. Kowalski, Z. Anorg. Allg. Chem. 224 (1935) 329–336;
(b) H. Harldsen, A. Neuber, Z. Anorg. Allg. Chem. 234 (1937) 353–371;
(c) K. Ozawa, T. Yoshimi, M. Irie, S. Yanagisawa, Phys. Stat. Sol. 11 (1972) 581–588;
(d) J.M. Leger, J.P. Bastide, Phys. Stat. Sol. 29 (1975) 107–113;
(e) M. Yuzuri, T. Kanomata, T.J. Kaneko, J. Magn. Magn. Mater. 70 (1987) 223–224;
(f) K. Hatakeyama, T. Kaneko, H. Yoshida, S. Ohta, S. Anzai, J. Magn. Magn. Mater. 90–91 (1990) 175–176;
(g) T. Kanomata, Y. Sugawara, K. Kamishima, H. Mitamura, T. Goto, S. Ohta, T. Kaneko, J. Magn. Magn. Mater. 177–181 (1998) 589–590;
(h) J. Dijkstra, H.H. Weitgering, C.F. van Bruggen, C. Haas, R.A. de Groot, J. Phys.: Condens. Matter 1 (1989) 9141–9161;
(i) J. Dijkstra, C.F. van Bruggen, C. Haas, R.A. de Groot, J. Phys.: Condens. Matter 1 (1989) 9163–9174.

[3] (a) M. Chevreton, M. Murat, C. Eyraud, J. Phys. 24 (1963) 443–446;
(b) A.W. Sleight, T.A. Bither, Inorg. Chem. 8 (1969) 566–569;
(c) M. Yuzuri, J. Phys. Soc. Japan 35 (1973) 1252;
(d) T. Kaneko, J. Sugawara, K. Kamigaki, S. Abe, H. Yoshida, J. Appl. Phys. 53 (1982) 2223–2225;
(e) Y. Adachi, M. Yuzuri, T. Kaneko, S. Abe, H. Yoshida, J. Phys. Soc. Japan 63 (1994) 369–370;
(f) Y. Adachi, M. Ohashi, T. Kaneko, M. Yuzuri, Y. Yamaguchi, S. Funahashi, Y. Morii, J. Phys. Soc. Japan 63 (1994) 1548–1559;
(g) T. Tsuji, K. Ishida, Thermochim. Acta 253 (1995) 11–18;
(h) F. Gronvold, J. Chem. Thermodyn. 5 (1973) 545–551.
[4] (a) H. Harldsen, A. Neuber, Naturwiss 24 (1936) 280;
(b) M. Yuzuri, Y. Nakamura, J. Phys. Soc. Japan 19 (1964) 1350–1354;
(c) T.J.A. Popma, C.F. Van Bruggen, J. Inorg. Nucl. Chem. 31 (1969) 73–80;
(d) K. Dwight, N. Menyuk, A. Kafalas, Phys. Rev. B 2 (1970) 3630–3633;
(e) T.J.A. Popma, C. Haas, B. van Laar, J. Phys. Chem. Solids 32 (1971) 581–590;
(f) D. Babot, M. Chevreton, J. Solid State Chem. 8 (1973) 166–174;
(g) M. Yuzuri, T. Kaneko, T. Tsushima, S. Miura, S. Abe, G. Kido, N. Nakagawa, J. Phys. C 8 (1988) 231–232;
(h) J. Hibble, R.I. Walton, D.M. Pickup, J. Chem. Soc. Daltons Trans. (1996) 2245–2251;
(i) P. Vaqueiro, A.V. Powell, A.I. Coldea, C.A. Steer, M.I. Marshall, S.J. Blundell, I. Singleton, T. Ohtani, Phys. Rev. B 64 (2001) 132402-1–132402-4.
[5] W. Bensch, O. Helmer, C. Näther, Mater. Res. Bull. 32 (1997) 305–318.
[6] K. Lukoschus, S. Kraschinski, C. Näther, W. Bensch, J. Solid State Chem. 177 (2004) 951–959.
[7] H. Huppertz, H. Luehmann, W. Bensch, Z. Naturforsch. 58b (2003) 934–938.
[8] W. Bensch, H. Luehmann, C. Näther, H. Huppertz, Z. Kristallogr. 217 (2002) 510–514.
[9] Z.-L. Huang, W. Bensch, D. Benea, H. Ebert, J. Solid State Chem. 177 (2004) 3245–3253.
[10] Z.-L. Huang, W. Bensch, D. Benea, H. Ebert, J. Solid State Chem. 178 (2005) 2778–2790.
[11] J. Rodriguez-Carvajal, Fullprof. 2k, Version 2.0c, July 2002/Lab. Leon Brillouin, 2002.
[12] J. Korringa, Physica 13 (1947) 392–400.
[13] W. Kohn, N. Rostoker, Phys. Rev. 94 (1954) 1111–1120.
[14] H. Ebert, et al., The Munich SPR-KKR package, version 2.1.1, http://olymp.cup.uni-meunchen.de/ak/ebert/SPRKKR.
[15] H. Ebert, in: H. Dressé (Ed.), Electronic Structure and Physical Properties of Solids, Springer, Berlin, 2000, pp. 191–246.
[16] S.H. Vosco, L. Wilk, M. Nusair, Can. J. Phys. 58 (1980) 1200.
[17] P. Soven, Phys. Rev. 156 (1987) 809–813.
[18] G.M. Stocks, W. Temmerman, B.L. Györffy, Phys. Rev. Lett. 41 (1980) 1200–1211.
[19] A.I. Lichtenstein, M.I. Katsnelson, V.P. Antropov, V.A. Gubanov, J. Magn. Magn. Mater. 67 (1987) 65.
[20] M. Paida, J. Kudrnovsky, I. Turek, V. Drchal, Phys. Rev. B 64 (2001) 174402.
[21] (a) W. Bensch, B. Sander, O. Helmer, C. Näther, F. Tuczek, A.I. Shames, A.M. Panich, J. Solid State Chem. 145 (1999) 235–246;
(b) W. Bensch, B. Sander, R.K. Kremer, W. Kockelmann, J. Solid State Chem. 158 (2001) 198–207.
[22] K. Shimada, T. Saitoh, H. Namatame, A. Fujimori, S. Ishida, S. Asano, S. Anzai, Phys. Rev. 53 (1996) 7673–7683.
[23] J.A. Mydosh, Spin Glasses: An Experimental Introduction, Taylor & Francis, London, 1993.
[24] (a) X.G. Li, X.J. Fang; G. Ji, W.B. Wu, K.H. Wong, C.L. Choy, H.C. Ku, J. Appl. Phys. 85 (1999) 1663–1666;
(b) S. Mukherjee, R. Ranganathan, P.S. Anikumar, P.A. Joy, Phys. Rev. 54 (1996) 9267–9274;
(c) D.N.H. Nam, K. Jonason, P. Nordblad, N.V. Khiem, N.X. Phuc, Phys. Rev. B 59 (1999) 4189–4194;
(d) M. Koyano, M. Suezawa, H. Watanabe, M. Inoue, J. Phys. Soc. Japan 63 (1994) 1114–1122;
(e) A. Maignan, C. Martin, F. Damay, B. Raveau, Phys. Rev. 58 (1998) 2758–2763;
(f) D.A. Pejakovic, J.L. Manson, J.S. Miller, A.J. Epstein, J. Appl. Phys. 87 (2000) 6028–6030;
(g) D.A. Pejakovic, J.L. Manson, J.S. Miller, A.J. Epstein, Phys. Rev. Lett. 85 (2000) 1994–1997.
[25] J.P. Perdew, K. Burke, M. Ernzerhof, Phys. Rev. Lett. 77 (1996) 3865.